Wind and Structures, Vol. 5, No. 2~4 (2002) 379-392
DOI: http://dx.doi.org/10.12989/was.2002.5.2_4.379

Numerical flow computation around aeroelastic 3D square cylinder using inflow turbulence

Hiroto Kataoka†

Technical Research Institute, Obayashi Corporation, 4-640 Shimokiyoto, Kiyose-shi, Tokyo 204-8558, Japan

Minoru Mizuno‡

Department of Environmental Engineering, Osaka University, 2-1 Yamadaoka, Suita-shi, Osaka 565-0871, Japan

Abstract. Numerical flow computations around an aeroelastic 3D square cylinder immersed in the turbulent boundary layer are shown. Present computational code can be characterized by three numerical aspects which are 1) the method of artificial compressibility is adopted for the incompressible flow computations, 2) the domain decomposition technique is used to get better grid point distributions, and 3) to achieve the conservation law both in time and space when the flow is computed a with moving and transformed grid, the time derivatives of metrics are evaluated using the time-and-space volume. To provide time-dependant inflow boundary conditions satisfying prescribed time-averaged velocity profiles, a convenient way for generating inflow turbulence is proposed. The square cylinder is modeled as a 4-lumped-mass system and it vibrates with two-degree of freedom of heaving motion. Those blocks which surround the cylinder are deformed according to the cylinder's motion. Vigorous oscillations occur as the vortex shedding frequency approaches cylinder's natural frequencies.

Key words: aeroelastic problem; 3D square cylinder; turbulent boundary layer; computational fluid dynamics; domain decomposition technique; moving and transformed grid; generating inflow turbulence.

1. Introduction

To investigate such aeroelastic motions as vortex induced vibration, galloping and flutter of tall buildings, wind tunnel tests have been carried out. The tests use scaled aeroelastic models of buildings. When the structural system becomes complicated or inelastic, it's hard to satisfy the dynamic similarity of building's motion.

The aeroelastic problem has become one of the crucial targets among the computational fluid dynamics (CFD) community (Tamura 1988). If the objective structure is isolated and its deformation is negligible compared to the displacement, the computation can be done simply by moving the whole computational domain in accordance with the structure's motion. This simplification makes it quite straightforward for researchers to adapt their existing flow-solvers to aeroelastic problems.

† Dr. Eng., Chief Research Engineer
‡ Professor

However, in the case of buildings, whole bodies do not sway horizontally but get deformed by wind forces since they are fixed at the ground level. So, to predict broader phenomena, the grid system should be transformed and deformed according to the buildings' motions and deformations.

The buildings are immersed in the boundary layer so, to get flow fields depending on time, fluctuating velocity profiles (the inflow turbulence) should be prescribed at each time step as inflow boundary conditions. There are two ways to enable us to generate the inflow turbulence; random fluctuation inflow generation methods (Kondo *et al*. 1998, Maruyama, Y. and Maruyama, T. 1999), or computed boundary layer flows using the results as inflows. With the former approach, the generated inflow can satisfy prescribed statistics but it requires detailed measurements of the target boundary layer flow. With the latter method, it had been hard to reproduce prescribed velocity profiles until Lund and his coworkers reported their way for spatially-developing boundary layer simulations (Lund *et al*. 1998). The most advantageous point with that approach is that the generated inflow conditions have the coherent structures of turbulent boundary layer flows whereas the former approach does not.

In this paper the authors would like to introduce a numerical method for computing flows around an aeroelastic 3D square cylinder. The method of artificial compressibility (Chorin 1967, Rogers *et al*. 1991, Kataoka and Mizuno 1998) is adopted for the incompressible flow computations and the basic equations are transformed into a generalized coordinate system. To get better grid point distributions around the cylinder, the domain decomposition technique (Kataoka and Mizuno 1997) is used. The computational domain is divided into blocks and some of these blocks are used for generating inflow turbulence or transformed and deformed after the building's motions and deformations. To fulfill the conservation laws both in time and in space when the flow is computed with a moving and transformed grid, time derivatives of metrics are computed according to the geometrical explanations (Tamura and Fujii 1993). For generating inflow turbulence, a simplified version of Lund's approach is applied. The generated profiles are compared with wind tunnel measurements to evaluate the present method. Then computed results of an aeroelastic square cylinder using generated inflow turbulence are shown.

2. Computational method

2.1. Governing equations

With the idea of artificial compressibility (Chorin 1967), the governing equations for unsteady incompressible flows can be written as (Rogers *et al*. 1991),

$$\begin{aligned} &\frac{\partial p}{\partial \tau} + \beta \mathrm{div}\,\mathbf{u} = 0 \\ &\frac{\partial \mathbf{u}}{\partial \tau} + \frac{\partial \mathbf{u}}{\partial t} = -(\mathbf{u}\cdot \mathrm{grad})\mathbf{u} - \mathrm{grad}\ p + \nu\nabla^2\mathbf{u} \end{aligned} \tag{1}$$

where $\mathbf{u} = (u_1, u_2, u_3) = (u, \upsilon, w)$, t is a physical time, τ is an artificial time, β is an artificial compressibility parameter and p denotes the pressure divided by the fluid's density ρ. Firstly, these equations are advanced in artificial time until the artificial time derivatives satisfy a convergence criterion. After that, they are advanced in physical time. The convergence criterion for the artificial time step is set at 10^{-4}, meaning that the continuity equation for incompressible flow is satisfied within an accuracy of 10^{-4} at each physical time step.

These equations are transformed from the Cartesian coordinate $(x_1, x_2, x_3, t) = (x, y, z, t)$ to the generalized one $(\xi_1, \xi_2, \xi_3, t) = (\xi, \eta, \zeta, t)$ as follows,

$$\frac{\partial \hat{Q}}{\partial \tau} + I_m \frac{\partial \hat{Q}}{\partial t} = \hat{R}$$

$$\hat{R} = -\frac{\partial(\hat{E}_c - \hat{E}_\upsilon)}{\partial \xi} - \frac{\partial(\hat{F}_c - \hat{F}_\upsilon)}{\partial \eta} - \frac{\partial(\hat{G}_c - \hat{G}_\upsilon)}{\partial \zeta}$$

$$\hat{Q} = \frac{1}{J}Q = \frac{1}{J}[p, u, \upsilon, w]^T \quad I_m = \mathrm{diag}[0, 1, 1, 1]$$

$$\hat{E}_{i_c} = \begin{bmatrix} \beta \hat{U}_i \\ \hat{\xi}_{ix} p + u\hat{U}_i + \hat{\xi}_{it} u \\ \hat{\xi}_{iy} p + \upsilon \hat{U}_i + \hat{\xi}_{it} \upsilon \\ \hat{\xi}_{iz} p + w\hat{U}_i + \hat{\xi}_{it} w \end{bmatrix} \qquad \hat{E}_{i_\upsilon} = 2\nu \begin{bmatrix} 0 \\ \hat{\xi}_{ix} S_{xx} + \hat{\xi}_{iy} S_{yx} + \hat{\xi}_{iz} S_{zx} \\ \hat{\xi}_{ix} S_{xy} + \hat{\xi}_{iy} S_{yy} + \hat{\xi}_{iz} S_{zy} \\ \hat{\xi}_{ix} S_{xz} + \hat{\xi}_{iy} S_{yz} + \hat{\xi}_{iz} S_{zz} \end{bmatrix} \qquad \begin{array}{l} \hat{E}_i = \hat{E}, \hat{F}, \hat{G} \\ \text{for } \ i = 1, 2, 3 \end{array}$$

$$\hat{\xi}_{ix_j} = \frac{1}{J}\xi_{ix_j} = \frac{1}{J}\frac{\partial \xi_i}{\partial x_j} \quad \hat{\xi}_{it} = \frac{1}{J}\xi_i = \frac{1}{J}\frac{\partial \xi_i}{\partial t} \quad J = \left|\frac{\partial(\xi, \eta, \zeta)}{\partial(x, y, z)}\right|$$

$$\hat{U}_i = \hat{\xi}_{ix} u + \hat{\xi}_{iy} \upsilon + \hat{\xi}_{iz} w \quad S_{x_i} S_{x_j} = \frac{1}{2}\left(\frac{\partial u_j}{\partial x_i} + \frac{\partial u_i}{\partial x_j}\right) \tag{2}$$

2.2. Discretization schemes

2.2.1. Spatial derivatives

The equations are discretized using a finite volume method (FVM). Definitions in detail can be found in the authors' paper (Kataoka and Mizuno 1997). The spatial derivatives of the convective and viscous flux vectors are discretized as follows

$$\frac{\partial \hat{E}_c}{\partial \xi} = (\hat{E}_c)_{i+1/2} - (\hat{E}_c)_{i-1/2} \qquad \frac{\partial \hat{E}_v}{\partial \xi} = (\hat{E}_v)_{i+1/2} - (\hat{E}_v)_{i-1/2} \tag{3}$$

where i is a spatial index. Viscous fluxes are computed with a second-order central difference. Physical variables at the node-centers (with indexes i+1/2 and i-1/2) are given by averaging grid points' values, and non-linear terms are approximated by a fourth-order central differencing plus a fourth-order damping term as,

$$\begin{aligned}(\mathbf{u}\hat{U})_{i+1/2} = {} & \frac{1}{12}\hat{U}_{i+1/2}(-\mathbf{u}_{i+2} + 7\mathbf{u}_{i+1} + 7\mathbf{u}_i - \mathbf{u}_{i-1}) \\ & -\frac{\alpha}{12}\left|\hat{U}_{i+1/2}\right|(-\mathbf{u}_{i+2} + 3\mathbf{u}_{i+1} - 3\mathbf{u}_i + \mathbf{u}_{i-1})\end{aligned} \tag{4}$$

α is a parameter for controlling the size of artificial dissipation term and is set as 0.5 (see Kataoka and Mizuno 1998). To avoid numerical pressure oscillations, a fourth-order damping term is added also to the pressure equation using the artificial speed of sound $\hat{c}_i$.

$$(\beta\hat{U})_{i+1/2} = \beta\hat{U}_{i+1/2} - \frac{\alpha}{12}\left(\left|\hat{U}_i + \frac{1}{2}\hat{\xi}_{it}\right| + \hat{c}_i\right)_{i+1/2}(-p_{i+2} + 3p_{i+1} - 3p_i + p_{i-1})$$

$$\hat{c}_i = \sqrt{(\hat{U}_i + \hat{\xi}_{it}/2)^2 + \beta(\hat{\xi}_{ix}^2 + \hat{\xi}_{iy}^2 + \hat{\xi}_{iz}^2)} \tag{5}$$

2.2.2. Moving and transformed grid and time derivatives

For the moving and transformed grid, the grid movement changes the control volume size in time, which makes it impossible to execute temporal and spatial integration separately. For example, if time derivatives of metrics $\hat{\xi}_{it}$ are computed with a chain rule as $\hat{\xi}_t = -\hat{\xi}_x x_t - \hat{\xi}_y y_t - \hat{\xi}_z z_t$, the geometrical conservation law Eq. (6) (Thomas and Lombard 1979) will not be satisfied.

$$\frac{\partial}{\partial t}\left(\frac{1}{J}\right) + \frac{\partial\hat{\xi}_t}{\partial\xi} + \frac{\partial\hat{\eta}_t}{\partial\eta} + \frac{\partial\hat{\zeta}_t}{\partial\zeta} = 0 \tag{6}$$

Hence they must be obtained by the way which treats both time and space at once. Rosenfeld and Kwak (1991) showed the geometrical way for computing $\hat{\xi}_{it}$. Tamura and Fujii (1993) explained its geometrical meanings in time and space dimensions. We took their geometrical interpretation for computing $\hat{\xi}_{it}$.

Taking a first-order explicit formula for the artificial time derivatives and a first or second-order implicit for the physical time derivatives, Eq. (2) yields the following discretized equations,

$$\left(\frac{1}{\Delta\tau} + \frac{I_m}{\Delta t}\right)V^{n+1}(Q^{n+1,m+1} - Q^{n+1,m}) = \hat{R}^m - \frac{I_m}{\Delta t}\{V^{n+1}Q^{n+1,m} - (VQ)^n\}$$

$$\left(\frac{1}{\Delta\tau} + \frac{3I_m}{2\Delta t}\right)V^{n+1}(Q^{n+1,m+1} - Q^{n+1,m})$$

$$= \hat{R}^m - \frac{I_m}{2\Delta t}\{3V^{n+1}Q^{n+1,m} - 4(VQ)^n + (VQ)^{n-1}\} \tag{7}$$

where $V = J^{-1}$, the superscripts n and m denote the quantities at physical time level $t = n\Delta t$ and the artificial time level $\tau = m\Delta\tau$, respectively. The pseudo-time step size $\Delta\tau$ is computed locally with a cell-Courant number CFL as (Kataoka and Mizuno 1998),

$$\Delta\tau = \mathrm{CFL} \times \frac{4}{J(\hat{\gamma}_\xi + \hat{\gamma}_\eta + \hat{\gamma}_\zeta)} \qquad \hat{\gamma}_{\xi_i} = \left|\hat{U}_i + \frac{1}{2}\hat{\xi}_{it}\right| + \hat{c}_i \tag{8}$$

2.2.3. Domain decomposition

Grid systems used for CFD can be classified into two different types depending on the underlying grid topology; Unstructured or Structured. With the domain decomposition technique, it is possible to take a hybrid approach with those grid systems. Thus, if the computational domain is divided into several blocks, the block level unstructured system would make it easier to control the grid point distribution around the bodies. Compared with the unstructured grid system, the grid level structured system is advantageous in formulating the discretization schemes. The discretization technique for adopting the domain decomposition is straightforward and can be found in the authors' paper (Kataoka and Mizuno 1997).

2.3. Generation of inflow turbulence

2.3.1. A technique proposed by Lund et al.

Lund *et al*. (1998) proposed a convenient way for generating inflow turbulence with parallel flow computations. They put a driver section at the windward position of the main domain, compute both flow fields simultaneously, extract flow fields from the driver section, and use them as inflows for the main domain. A periodic boundary condition is set for both spanwise and streamwise directions of the driver, while only the fluctuating part of the velocity was recycled in the streamwise direction. The fluctuating part can be computed as,

$$\mathbf{u}'(x, y, z, t) = \mathbf{u}(x, y, z, t) - \langle\mathbf{u}\rangle(x, z) \tag{9}$$

where x is streamwise, y is spanwise and z is wall-normal direction respectively. The mean value $\langle\mathbf{u}\rangle$ is obtained by averaging in spanwise and time directions. Since the boundary layer thickness develops in the streamwise direction, the fluctuating part must be scaled between the inlet (*inlt*) and the downstream (*recy*) planes of the driver section as,

$$\mathbf{u}'_{inlt} = \chi \mathbf{u}'_{recy}(y, z^+_{inlt}, t) \qquad \chi = u^*_{inlt}/u^*_{recy} \tag{10}$$

where $z^+ = u^* z / v$ is the wall coordinate and u^* is the friction velocity. Furthermore, $\mathbf{u}'_{inlt}$ needs to be interpolated along the z direction to be the same z^+ as the inlet.

The most characteristic point with this method is that the fluctuating part of the velocity is recycled instead of the instantaneous velocity itself. By adding the fluctuations to the mean velocity profiles at the inlet section, time depending inflow velocities can be generated, and still their time averaged values are the same as prescribed values.

2.3.2. Method simplification

The authors simplified Lund's method by assuming that the boundary layer thickness is constant within the driver section. By this assumption, scaling parameter χ and interpolations are not necessary any more. Then following relations are derived,

$$\begin{aligned} u_{inlt}(y, z, t) &= \langle u\rangle_{inlt}(z) + \phi(\theta)\times \{u_{recy}(y, z, t) - [u](z)\} \\ \upsilon_{inlt}(y, z, t) &= \phi(\theta)\times \upsilon_{recy}(y, z, t) \\ w_{inlt}(y, z, t) &= \phi(\theta)\times \{w_{recy}(y, z, t) - [w](z)\} \end{aligned} \tag{11}$$

where $\theta = z/\delta$, δ is the boundary layer thickness, $[u]$ and $[w]$ are the averaged values in horizontal plane and $\langle u\rangle_{inlt}$ is the specified mean profile. Contrary to the initial assumption, the boundary layer thickness develops unavoidably. $\phi(\theta)$ is a damping function to block the velocity fluctuation from developing in the free stream.

3. Computed results

3.1. 3D flow computations over a 2D square cylinder

3D flow computations over a fixed 2D square cylinder at Reynolds number 22¸000 (based on the cylinder's diameter D and free stream velocity u_0) has been conducted (Kataoka and Mizuno 1998).

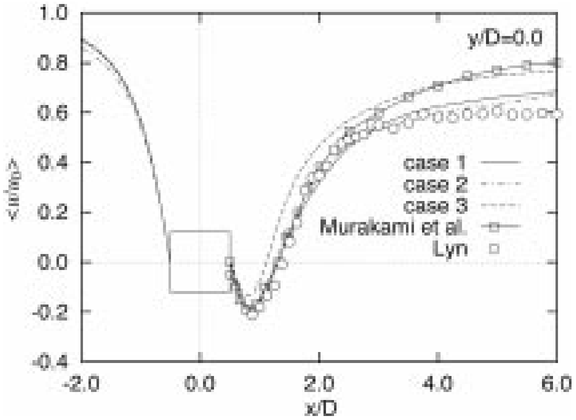

Fig. 1 Comparison of the time averaged streamwise velocity distributions. Computations (case 1-3) are based on different grid resolutions (case 2 is the finest and case 3 is the coarsest)

Computations were done without any turbulence models and the physical time derivatives are treated as a second-order.

Fig. 1 compares the time averaged streamwise velocity $<u / u_0>$ distributions along the symmetry line from the present computations (cases 1, 2 and 3), LES computation based on the dynamic mixed SGS model (Murakami *et al*. 1997) and experimental data (Lyn and Rodi 1994), where u is the streamwise (x direction) velocity and < > denotes time averaged values. In the wake flow, case 1, 2 and LES results show a very good agreement with the experimental data while case 3 underestimates the size of recirculation due to the grid coarseness. Though present computations are laminar, they show the same accuracy as Murakami's LES computation (or even closer to experimental data in the far wake region). The figure proves that the artificial compressibility method can predict the separating flow.

3.2. Generated turbulent boundary layer

To confirm the present technique for generating inflow turbulence, a turbulent boundary layer flow computation is conducted. As a reference, wind tunnel measurements of flow around a square cylinder ($D = 0.08$ m, $H = 0.16$ m, $U_H = 4.491$ m/s, $Re = U_H D / \nu = 24{,}000$, $\delta = 0.6$ m) conducted by Meng and Hibi (1998) are chosen. The experimental mean flow profile is shown in Fig. 2. By fitting to the log law (Fig. 3), the friction velocity is estimated as 0.17 m/s ($Re_\tau = u^* \delta / \nu = 6{,}800$). The target mean profile is set as,

$$
\begin{aligned}
&<u> / u^* = z^+ = zu^* / \nu && && z^+ < 5 \\
&<u> / u^* = 2.5 \ln z^+ + 5.5 && 30 < z^+ && z < z_1 \\
&<u> / U_H = \min\{(z / H)^{0.33}, 1.5\} && && z_1 < z
\end{aligned}
\tag{12}
$$

where the power law profile succeeds the log law at z_1 (about $1.3D$). The domain size is $10D \times 13.5D \times 11D$ in streamwise, spanwise and vertical direction respectively, and divided into $21 \times 55 \times 45 = 51{,}945$ grid points (see Block 6 in Fig. 8). Grid points are stretched into the floor with the minimum distance as $z^+ = 1.1$. Computational conditions are, $\Delta t U_H / D = 0.01$, $\beta = 100$, CFL = 2.0, second-order differences for the physical time derivatives, a free slip boundary condition

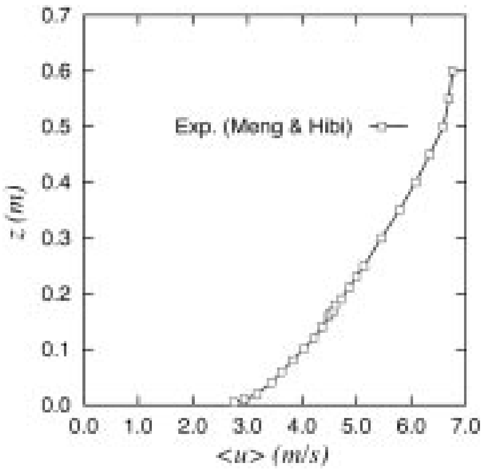

Fig. 2 Measured mean velocity profile

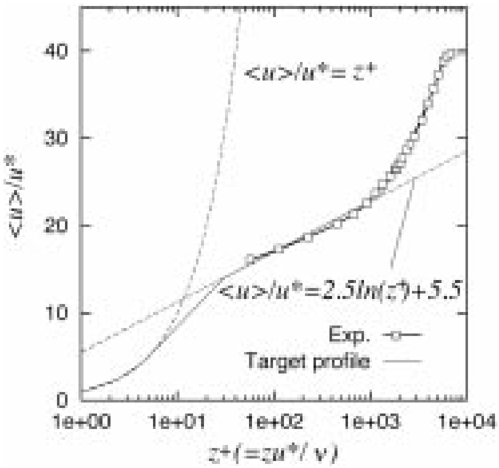

Fig. 3 Measured profile (in log scale)

for the ceiling, a periodic condition for side walls, a no-slip condition for the floor, and turbulence models are not included.

Figs. 4-7 show generated profiles with the measurements. They are computed from the instantaneous data of $\Delta t U_H / D = 800$ to 1,200. The generated mean velocity becomes slightly faster at the log law region and slower at the top, however, the specified velocity profile is well reproduced (Fig. 4). It is interesting that the generated fluctuations (Fig. 5) show better agreement with measurements though there was no numerical control for them. This coincidence suggests there could be a cause-and-effect relation between the mean and fluctuating velocity profiles. Fig. 7 shows the power spectrum of velocities at $(y, z) = (0, H)$ of the outflow plane. The power drops steeply at about $nD / U_H = 1.0$, which is the finest frequency defined by streamwise grid size and U_H. A power peak appears at about $nD / U_H = 0.1$ because of the streamwise size of the domain.

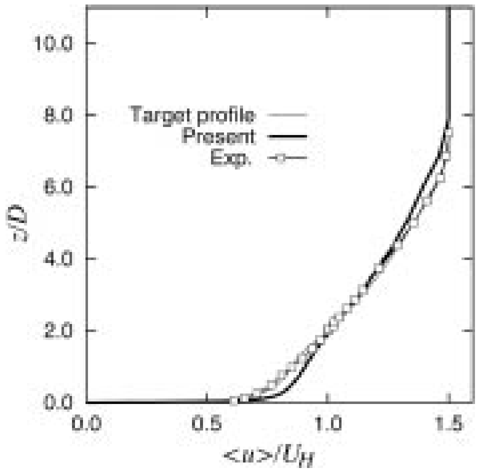

Fig. 4 Generated mean velocity profile

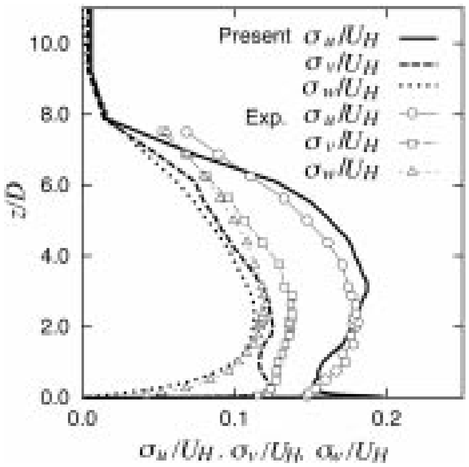

Fig. 5 Generated velocity fluctuations

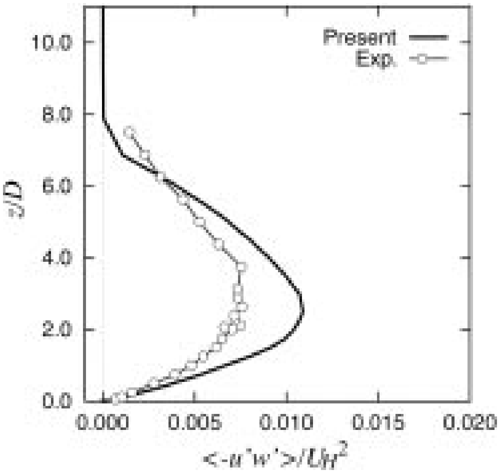

Fig. 6 Generated Reynolds stress

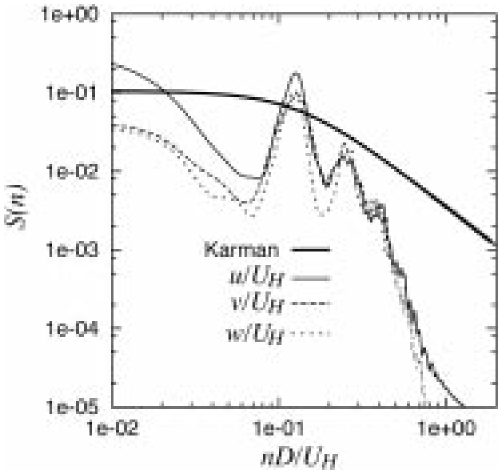

Fig. 7 Power spectra of generated velocities

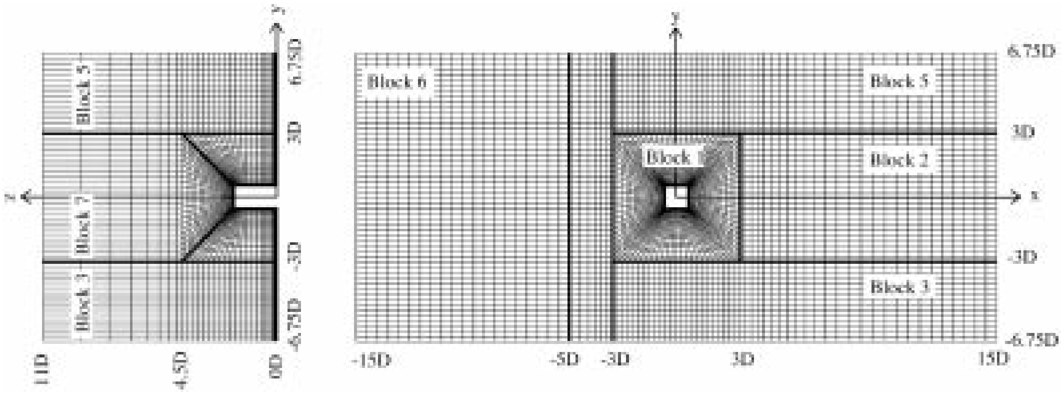

Fig. 8 Grid system for the square cylinder (7 blocks, 308,749 grid points)

The flow computation around a square cylinder is carried out using generated inflow conditions and results are compared with Meng and Hibi's measurements also. Fig. 8 shows the grid system. The domain is divided into 7 blocks and inflow conditions are generated within the block 6. The computational conditions are the same as before, but a free slip condition is applied for side wall boundaries except block 6.

Figs. 9 and 10 compare the computed results with the measurements. The computed velocity profiles are in good accordance with experiments (Fig. 9), and computed velocity fluctuations show modest coincidence (Fig. 10). Sub-grid scale (SGS) turbulence models which are not included in the computation are expected to improve the solution. As reported by Jordan (1999), however, the combination of filtering operation and coordinate transformation is still under investigation. Yet SGS models working with the moving and transformed grid system are not investigated. Since the upwind difference scheme is used for convective terms, the present computation cannot be called as a DNS.

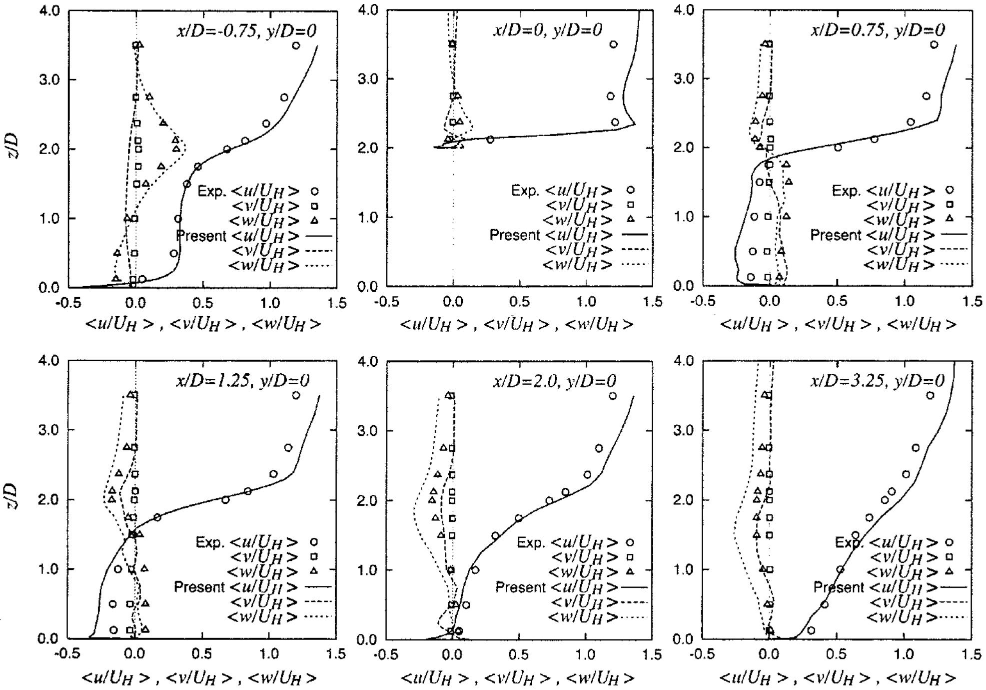

Fig. 9 Time averaged velocity profiles within $y / D = 0$ section

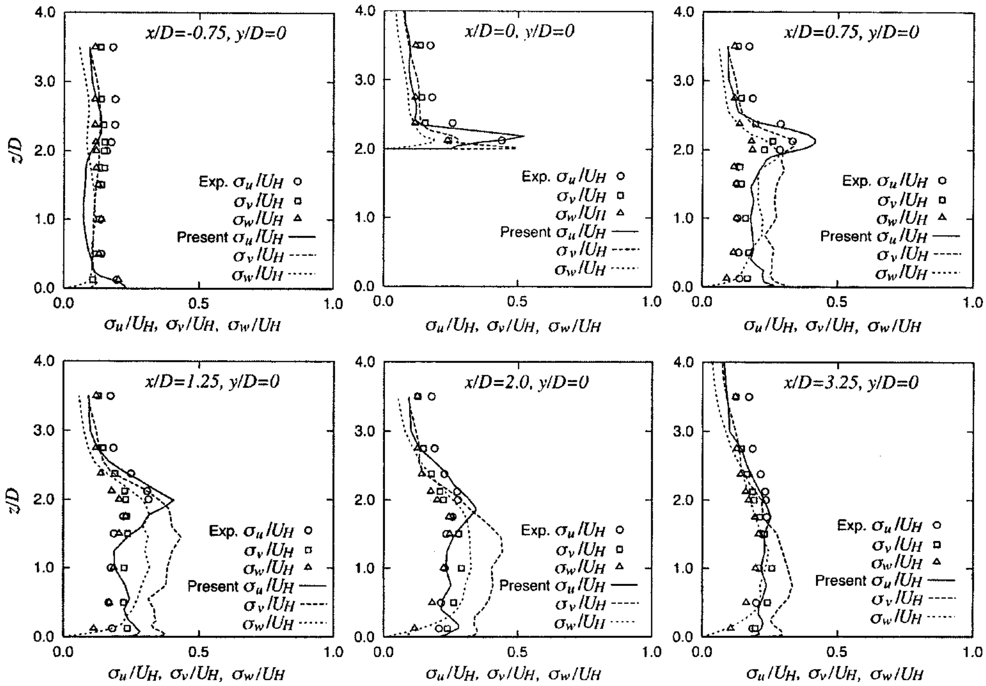

Fig. 10 Fluctuating velocity profiles within $y / D = 0$ section

3.3. Aeroelastic 3D square cylinder

Fig. 11 shows the model for the aeroelastic square cylinder. It is modeled as a 4-lumped-mass system and vibrates with two-degrees of freedom of heaving motion. Its density ratio is $(\rho_m / \rho = 100)$. The stiffness and the damping ratio are constantly distributed. Fig. 12 shows the normalized modes of vibration. The cylinder's motion can be defined as follows,

$$\frac{d\mathbf{a}}{dt} = \mathbf{a}' \quad \frac{d\mathbf{a}'}{dt} = \mathbf{M}^{-1}(\mathbf{F} - \mathbf{C}\mathbf{a}' - \mathbf{K}\mathbf{a}) \tag{13}$$

where **a** and **a′** are displacement and oscillation velocity vectors, **M**, **F**, **C**, **K** are mass, wind force, damping and stiffness matrices respectively. Eq. (13) is integrated by a 5-step Runge Kutta method. Computations are conducted with 4 reduced velocity conditions as listed in Table 1. The mechanical damping ratio based on the 1st natural vibration mode is about 0.6%.

The grid system is shown in Fig. 13. The domain is divided into 7 blocks and blocks 1 and 7 are transformed after the cylinder's motion. Block 6 is a driver section for generating inflow turbulence. The computational conditions are, $Re = U_H D / \nu = 2{,}700$, $\Delta t U_H / D = 0.01$, $\beta = 100$, CFL = 2.5 and first-order differences for the physical time derivatives. The boundary conditions are the same as in the 3D fixed cylinder case. The target velocity profiles are set as Eq. (14) where $z^+ = zRe_\tau / \delta$, $Re_\tau = 1{,}280$ and $\delta = 10D$. In Fig. 14, the generated profiles are shown.

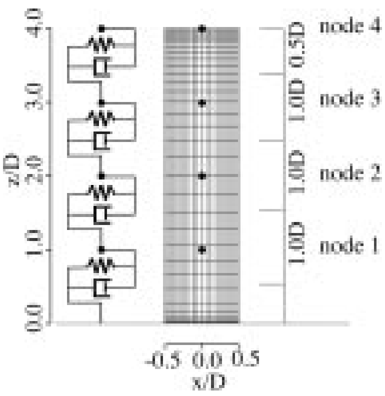

Fig. 11 Model for aeroelastic cylinder

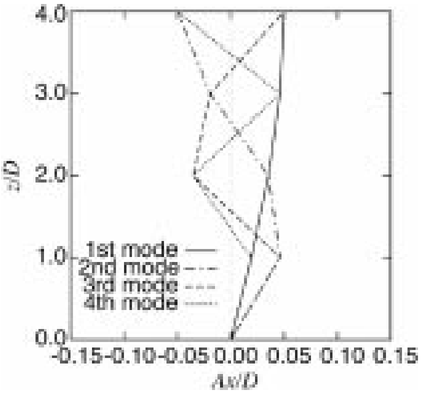

Fig. 12 Vibration modes

Table 1 Computational conditions for aeroelastic cylinder

Vr	Mode frequencies			
	1st	2nd	3rd	4th
$U_H / f_1 D$	$f_1 D / U_H$	$f_2 D / U_H$	$f_3 D / U_H$	$f_4 D / U_H$
6.4	0.156	0.445	0.664	0.785
8.6	0.117	0.333	0.499	0.589
12.8	0.078	0.222	0.333	0.192
25.6	0.039	0.111	0.166	0.196

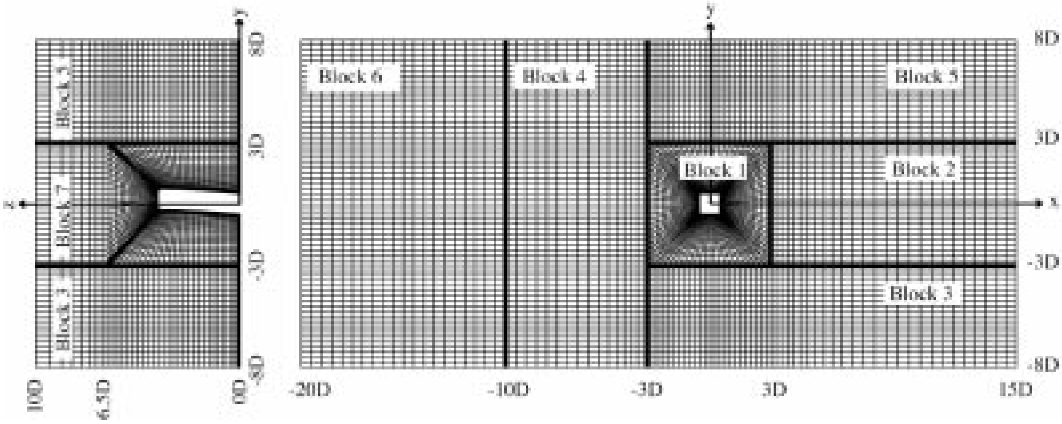

Fig. 13 Grid system for aeroelastic cylinder (7 blocks, 332,721 grid points)

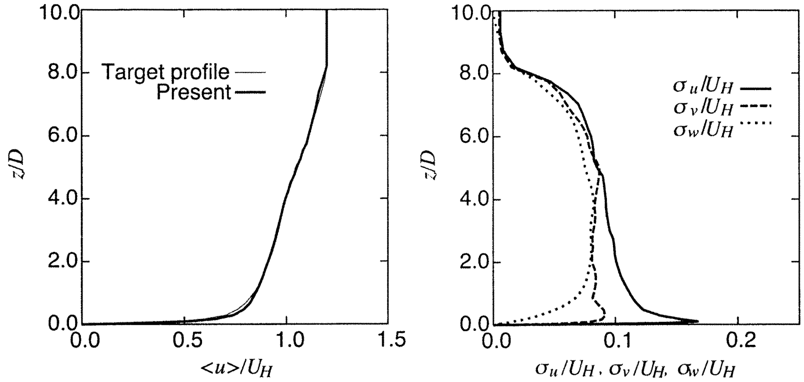

Fig. 14 Inflow velocity profiles (left: time averaged, right: fluctuation)

$$
\begin{aligned}
&\langle u\rangle/u^* = z^+ && z^+ < 5 \\
&\langle u\rangle/u^* = 2.5\ln z^+ + 5.5 && 30 < z^+ \quad z < H \\
&\langle u\rangle/U_H = \min\{(z/H)^{0.266},\ 1.2\} && z < H
\end{aligned}
\tag{14}
$$

Fig. 15 shows the cross-wind directional displacement of the node. At $Vr = 8.6$ and 25.6, vigorous oscillations occur. They are the cases when the vortex shedding resonates to the cylinder's first and second vibration mode. Their instantaneous vortical structures around the cylinder and power spectra of cross-wind force coefficient C_{Fy} are shown in Figs. 16, 17. Vortical structures are captured by visualising the second eigenvalue of the velocity gradient tensor (Jeong and Hussain 1995). The cross-wind force on the lower half of the cylinder is larger than on the higher part. This coincides with the experiments (Maruyama *et al.* 1996) qualitatively.

Fig. 18 shows the phase angles ϕ of C_{Fy}. As the wind speed increases, the positive phase angle, namely the negative aerodynamic-damping occurs along the whole span at the shedding frequency St ($Vr = 8.6$). Then the angle shifts about 180 degree as Vr approaches 12.8. This shift decreases the cross-wind displacement at $Vr = 12.8$. When the shedding approaches the second vibration mode ($Vr = 25.6$), negative damping occurs on the lower half and positive damping at the other part. So the wind forces activate the cylinder's oscillation on the lower part while the cylinder's motion at the top decelerates the vibration.

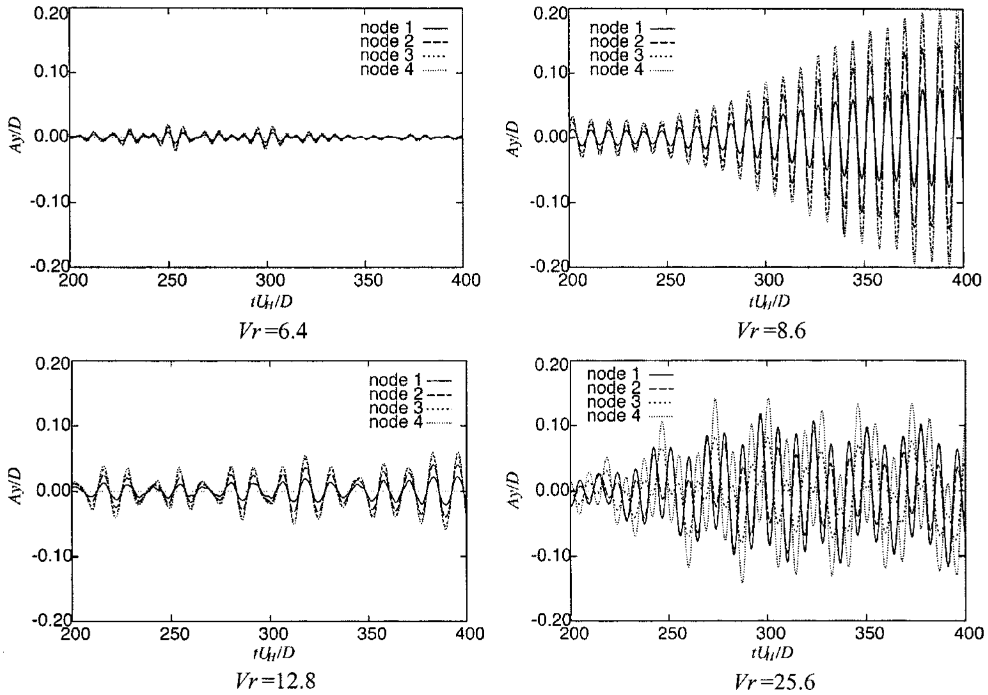

Fig. 15 Time history of cross-wind directional dislacement

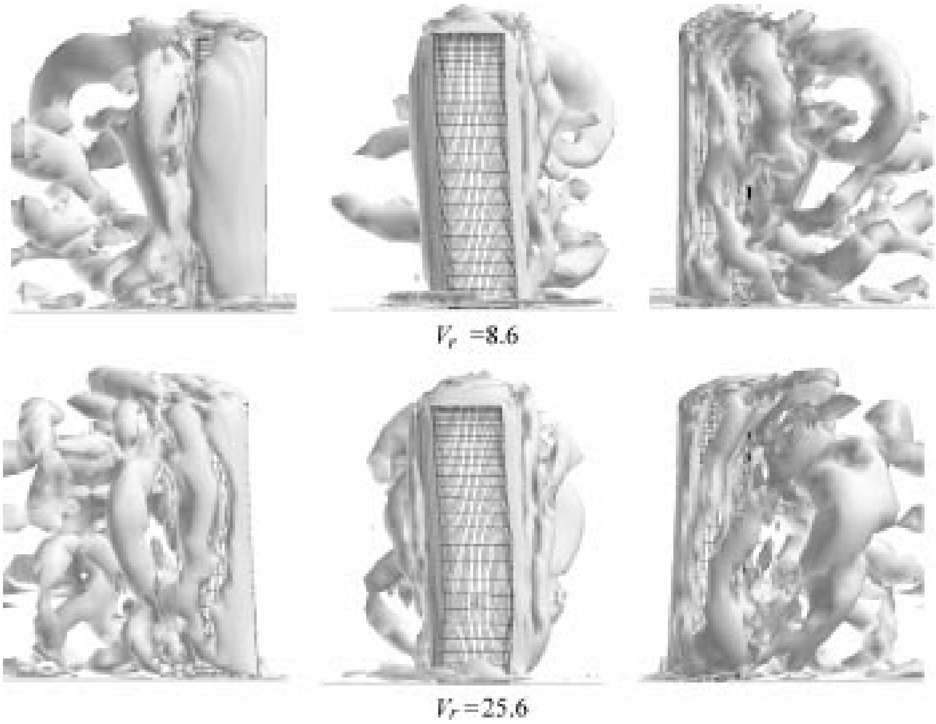

Fig. 16 Instantaneous vortical structures

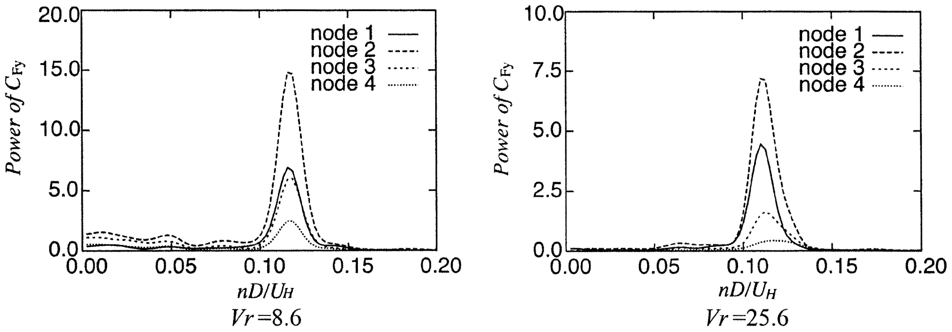

Fig. 17 Power spectra of C_{Fy}

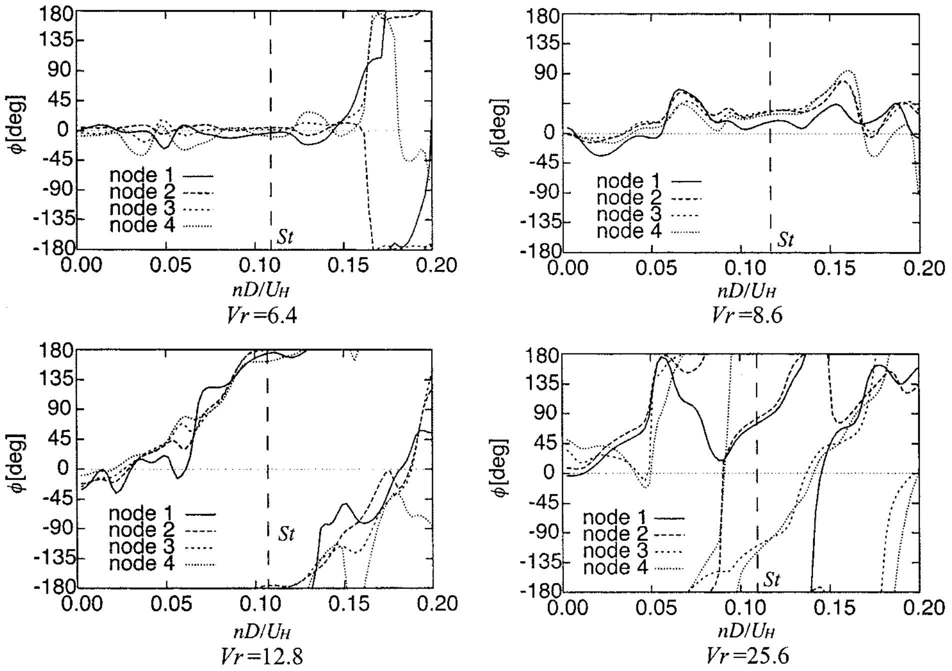

Fig. 18 Phase angle ϕ of C_{Fy}

4. Conclusions

The numerical method based on artificial compressibility, the domain decomposition technique and the conservation law, both in time and in space, is explained. To demonstrate the feasibility and benefits of the presented method, 3D flows around 2D and 3D square cylinders are computed. The results show that it can predict the separating flow either in the uniform flow or in the turbulent flow.

A convenient technique for generating inflow turbulence is proposed and is shown to reproduce the specified mean velocity profiles.

Then computed results for wind-induced oscillations of an aeroelastic square cylinder which is submerged in the turbulent boundary layer are provided. The results show the resonance at two reduced velocity conditions. When the vortex shedding resonates to the cylinder's second vibration mode, aerodynamic forces are found to activate the oscillation at the lower part, damping it at the top at the same time. Though computations are done at small Reynolds number (=2,700), the results show qualitative agreement with the experiments.

Since the present code does not include any turbulence models, the solution accuracy would be improved by them. When computing the flow around a 3D oscillating cylinder a moving and transformed grid should be used. The time-dependent transformation according to the cylinder motion provides the change of grid shape – i.e., the change of filter length in time for the SGS model. None of the existing SGS models account for this time dependent filter length and so some doubt must also attach to results using that approach, especially for aeroelastic problems.

On the other hand, the present results in Sections 3.1 and 3.2 show the same accuracy as LES or are in good agreement with experimental results. This is because

- the computed Reynolds Numbers are moderate (22-24,000),
- the grid systems have sufficient spatial resolution to capture those eddies that are essential to the separated flow, and
- by taking $\alpha = 0.5$ in Eq. (4) the effect of artificial damping is minimized.

References

Chorin, A.J. (1967), "A numerical method for solving incompressible viscous flow problems", *J. Comp. Physics*, **2**, 12-26.

Jeong, J. and Hussain, F. (1995), "On the identification of a vortex", *J Fluid. Mech.*, **285**, 69-94.

Jordan, S.A. (1999), "A Large-eddy simulation methodology in generalized curvilinear coordinates", *J. Comp. Physics*, **148**, 332-340.

Kataoka, H. and Mizuno, M. (1997), "Numerical method of multiblock computation for flow around complex building", *J. Archit. Plann. Environ. Eng., Trans. AIJ*, **495**, 53-60.

Kataoka, H. and Mizuno, M. (1998), "Numerical simulation of separating flow around a body using artificial compressibility method", *J. Archit. Plann. Environ. Eng., Trans. AIJ*, **504**, 63-70.

Kondo, K., Mochida, A., Murakami, S. and Tsuchiya, M. (1998), "Generation of inflow turbulence for LES of turbulent boundary layer (in Japanese)", *J. Struct. Constr. Eng., Trans. AIJ*, **509**, 33-40.

Lund, T.S. *et al*. (1998), "Generation of turbulent inflow data for spatially-developing boundary layer simulations", *J. Comp. Physics*, **140**, 233-258.

Lyn, D.A. and Rodi, W. (1994), "The flapping shear layer formed by flow separation from the forward corner of a square cylinder", *J. Fluid Mech.*, **267**, 353-376.

Maruyama, Y., Taniike, Y. and Nishimura, H. (1996), "Unsteady aerodynamic pressure on a high-rise building oscillating in the transverse direction (in Japanese)", *J. Struct. Constr. Eng., Trans. AIJ*, **504**, 31-37.

Maruyama, Y. and Maruyama, T. (1999), "Large eddy simulation of turbulent flow around a 3d-rectangular prism using artificially generated inflow (in Japanese)", *J. Struct. Constr. Eng., Trans. AIJ*, **520**, 37-43.

Meng, Y. and Hibi, K. (1998), "Turbulent measurements of the flow field around a high-rise building (in Japanese)", *J. Wind Eng.*, **76**, 55-64.

Murakami, S., Iizuka, S., Mochida, A. and Tominaga, Y. (1997), "LES analysis on turbulent flow past 2D square cylinder using various dynamic SGS models", *Seisan-Kenkyu*, **49**(1), 39-45.

Rogers, S.E., Kwak, D. and Kiris, C. (1991), "Steady and unsteady solutions of the incompressible Navier-Stokes equations", *AIAA J.*, **29**(4), 603-610.

Rosenfeld, M. and Kwak, D. (1991), "Time-dependent solutions of viscous incompressible flows in moving co-ordinates", *Int. J. Nmerical Methods in Fluids*, **13**, 1311-1328.

Tamura, T., Tsuboi, K. and Kuwahara, K. (1988), "Numerical simulation of unsteady flow patterns around a vibrating cylinder", *AIAA paper* 88-0128.

Tamura, Y. and Fujii, K. (1993), "Conservation law for moving and transformed grids", *AIAA paper* 93-3365.

Thomas, P.D. and Lombard, C.K. (1979), "Geometric conservation law and its application to flow computations on moving grids", *AIAA J.* **17**, 1030-1037.